Geophysical Journal International

Geophys. J. Int. (2025) **241,** 1822–1838
Advance Access publication 2025 April 17
GJI Geomagnetism and Electromagnetism

https://doi.org/10.1093/gji/ggaf121

Analysis of the seasonal and solar effect on the vertical magnetic transfer function at Eskdalemuir Observatory, Scotland

Guanren Wang [1,2] Juliane Hübert [1] and Kathryn A. Whaler [2]

[1] *British Geological Survey, The Lyell Centre, Research Avenue South, Edinburgh EH14 4AP, UK. E-mail: guanren@bgs.ac.uk*
[2] *School of GeoSciences, University of Edinburgh, King's Buildings, James Hutton Road, Edinburgh EH9 3FE, UK*

Accepted 2025 March 26. Received 2025 March 24; in original form 2024 May 8

SUMMARY

Geomagnetic observations at Eskdalemuir observatory in Southern Scotland reveal reduced amplitudes in the vertical component variations compared with the horizontal components for periods of less than an hour. A subsurface high conductivity feature has previously been suggested to account for this anomaly. However, past studies have overlooked the effect of seasonal source changes and impact of solar activity on external geomagnetic field variations. The vertical magnetic transfer function — referred to as the tipper — relates temporal variations in the vertical magnetic field to those in the horizontal magnetic field and is sensitive to lateral electrical conductivity contrasts in the subsurface. Quantifying the seasonal variations in the tipper helps to identify times when external field variations minimally bias tipper estimates, thereby providing a more accurate representation of subsurface conductivity. Ionospheric current systems, particularly during geomagnetic storms, may violate the plane wave assumption underlying tipper estimation at mid-latitudes. This may allude to a more complex source geometry responsible for magnetic field variations. Our study quantifies and proposes a correction for space weather-driven external field contributions to observations for periods shorter than 1 hr. Using high-quality digital magnetic field data with a 1-min sampling rate from 2001 to 2019, we estimate the tipper at Eskdalemuir, revealing seasonal differences that increase with periods between 1000 s and 10 000 s. After finding that tipper estimates during the 2016 time-series are least affected by seasonal effects, we used 1-s time-series and a simple empirical model to quantify the daily variability of the tipper. The model consists of annual and semi-annual terms plus a term proportional to either the $F10.7$ cm solar flux or geomagnetic A_p index. Neither model fits the data to within the expected error, but the model that uses A_p has better fit. Tipper estimates from temporary site deployments are affected by these seasonal external variations, and we correct those obtained at sites near Eskdalemuir during a recent field experiment using this model.

Key words: Geomagnetic induction; Magnetic field variations through time; Magnetotellurics; Time-series analysis.

1 INTRODUCTION

Solar activity expels streams of energetic particles that can impact the near-space environment and adversely affect the performance and reliability of technological systems (Baker 1998, Beedle *et al.* 2022). These collective effects are referred to as space weather. Intensification of magnetospheric–ionospheric currents during times of heightened space weather activity, such as geomagnetic storms and substorms, cause large and rapid variations of the magnetic field that are recorded by geomagnetic observatories (e.g. Beggan *et al.* 2024). Our interests here are the magnetic variations arising from electrical currents induced by external current systems diffusing into the Earth's conductive interior (Schmucker 1969). Permanent geomagnetic observatories such as the Eskdalemuir observatory (ESK) record variations in the total field magnetic field, consisting of internal (B_{int}) and external (B_{ext}) parts, with the internal field including an induced component.

The vertical magnetic transfer function — the so-called tipper — relates temporal variations in the vertical magnetic field to those in the horizontal magnetic field in the spectral domain. It is frequently used in magnetotelluric (MT) studies as a means to model the subsurface electrical conductivity at crustal and mantle depths. Barring any changes to the subsurface conductivity arising from geodynamic processes (Rokityansky *et al.* 2012), the tipper at a particular location is not expected to vary temporally. However, Takeda (1997) noted that even at mid-latitudes, the tipper is temporally varying and therefore not free from source effects, which are found to increase at longer periods and higher latitudes.

1.1 Vertical component geomagnetic anomaly at Eskdalemuir

Eskdalemuir is located in the Scottish Southern Uplands (Fig. 1). The Southern Uplands consist mostly of Silurian greywacke and other sedimentary deposits formed when the terrane was submerged under the Iapetus Ocean and experienced accretionary accumulation in the Caledonian orogeny with a NE-SW strike (Oliver *et al.* 2002). Sporadic distributions of igneous intrusions and volcanic lava are persistent throughout. Eskdalemuir has been the location of one of the UK's three permanent geomagnetic observatories and has operated since 1904 by the British Geological Survey.

The anomalous behaviour of the time-varying vertical magnetic field component (B_z) measured at ESK captured the intrigue of geophysicists over five decades ago (Jain & Wilson 1967; Osemeikhian & Everett 1968; Edwards *et al.* 1971; Jones & Hutton 1977; 1979; Parkinson & Jones 1979; Hutton *et al.* 1997). However, scientific interest dwindled after this peak in interest. Historical analogue and modern digital magnetic data from ESK (Fig. 2) reveal a dampened amplitude in B_z for periods less than an hour, compared to data from sites less than 80 km away (Edwards *et al.* 1971). The attenuation in amplitude is not observed in the horizontal intensity (Fig. 2). Known as the Eskdalemuir anomaly, there is not unanimous agreement as to what explains the dampened amplitude of B_z variations compared to those recorded at nearby sites. Bailey & Edwards (1976) proposed that the tectonic significance of the Eskdalemuir anomaly could be linked to closure of the Iapetus Ocean (Tauber *et al.* 2003).

1.2 Geomagnetic depth sounding and the tipper

At any fixed point on the Earth's surface, the geomagnetic field vector is a function of time and space, and can be resolved into its east–west (B_y) and north–south (B_x) components which together make up horizontal intensity, B_h. Geomagnetic depth sounding (GDS) uses the ratio of the time-dependent B_h and B_z in the spectral domain to derive the tipper (Schmucker 1969). The electromagnetic field penetrates the Earth to a depth dependent on frequency and conductivity, and this is utilized by GDS to detect conductivity gradients in the crust and upper mantle when applied to data from multiple sites (Chamalaun 1985).

The tipper, **T**, is a dimensionless vector, and a complex function of frequency (Schmucker 1969; Weidelt & Chave 2012) whose components are defined by

$$\widetilde{B}_z(f) = T_x\widetilde{B}_x(f) + T_y\widetilde{B}_y(f) + \epsilon(f), \tag{1}$$

where frequency $f = \frac{2\pi}{t}$ and t is the period. $\widetilde{B}_x$, $\widetilde{B}_y$ and $\widetilde{B}_z$ are the Fourier transforms at frequency f of B_x, B_y, B_z and $\epsilon(f)$ describes the spectral transform noise at frequency f. Elements T_x and T_y in eq. (1) represent the response to lateral conductivity variations. Using accurate estimates of the tipper (T_x, T_y) from an input of $\widetilde{B}_x$ and $\widetilde{B}_y$ for a discrete frequency, we can derive $\widetilde{B}_{z,\text{ind}}$ using eq. (1), where the subscript 'ind' indicates the induced component, assuming $\epsilon(f)$ is negligible (Chamalaun 1985; Hutton *et al.* 1997).

In electromagnetic induction, it is assumed that large-scale electrical current sheets are far away at low- to mid-latitudes such that B_{ext} can be approximated as spatially uniform plane waves impinging on the ground (Arora *et al.* 1999); as such, the tipper at any fixed period is approximately quasi-stationary. The implication is that the induced vertical magnetic field component anomalies are entirely due to subsurface lateral conductivity contrasts. If the conductivity distribution varies only with depth, the anomalous induced vertical magnetic field and the resulting tipper are zero.

On the basis of eq. (1), any changes in the external B_h due to processes in the ionosphere or beyond (source field) can induce anomalous magnetic field variations caused by lateral contrasts in the subsurface electrical conductivity (Schmucker 1969; Edwards *et al.* 1971; Ernst *et al.* 2020). This induced component contributes more significantly to B_z than the induced horizontal component does to B_h. Therefore, anomalous effects from lateral conductivity contrasts are more pronounced in variations of the B_z component (Schmucker 1969; Bailey & Edwards 1976), making variations in B_z useful for inferring conductivity structure. Sub-hourly B_z variations have been found to differ over distances of tens of kilometres, which is attributed to electrically conductive anomalies in the crust or upper mantle (Honkura 1978).

Previous studies have identified temporal variations in the tipper estimates that could be a result of the interaction of the source field with the subsurface conductivity structure, both analysed seasonally (Vargas & Ritter 2016; Maksymchuk *et al.* 2018; Anusha & Arora 2023) or day-time and night-time (Ernst *et al.* 2020). Source effects on the measured B_z, and hence the stationarity or stability of the tipper at ESK, have yet to be investigated as a possible contribution to the Eskdalemuir anomaly.

This study seeks to investigate the effects of space weather on B_z variations and on the tipper at ESK using long time-series of digital 1-s and 1-min data. The impact of seasonality on the tipper during the last solar cycle is analysed. We then identify the times at which the tipper appears to be least affected by source effects, which we subsequently refer to as a 'stable' tipper estimate. Temporary deployment of equipment to collect GDS and long-period magnetotelluric (LMT) data for induction studies does not provide the long time-series needed to compensate for effects from non-uniform ionospheric currents. A stable tipper from a long-running site such as ESK can be used to correct for seasonal effects on the tipper at nearby stations so that they are credible indicators of the subsurface conductivity.

The following section outlines the temporal resolution and length of magnetic time-series from ESK used in this study. A description of the processing software used to estimate tipper from such data is provided. Impacts on the tipper based on the choice of 3-months geomagnetic field variations affected by solar activities and used as input are analysed in Section 2.2. An empirical model developed by Vargas & Ritter (2016) that accounts for seasonal tipper variations observed throughout the year is discussed and augmented in Section 2.3. Modelling results, including corrections for source effects to the tipper estimated at temporary sites near ESK due to deviations from the plane wave assumption, are presented and discussed in Section 3 and Section 4. Conclusions are summarized in Section 5.

2 METHODOLOGY

2.1 Derivation of the tipper at ESK from magnetic field data

The British observatories LER, HAD and ESK (Fig. 1) produce accurate long-term records of full field geomagnetic data sampled at 1 s and 1 min in real time (Clarke *et al.* 2013). In this study, minute mean values of B_x, B_y and B_z from ESK between 2001

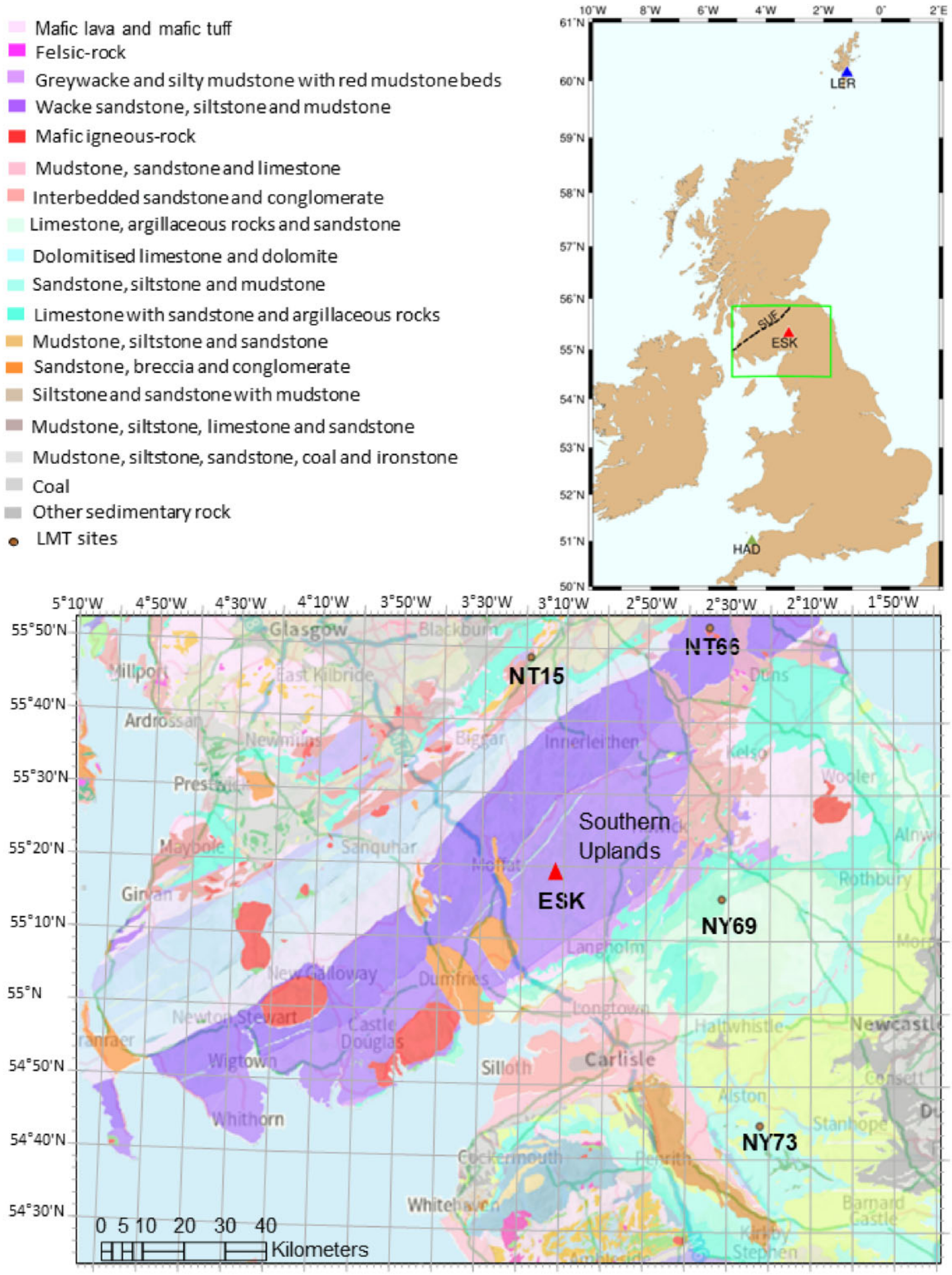

Figure 1. Location of sites and geology of Southern Scotland, adapted from maps produced by the British Geological Survey. The Eskdalemuir observatory (ESK) is indicated by the red triangle and nearby Long-period Magnetotelluric (LMT) sites are indicated by the dots. Top figure shows the location of the three British Geomagnetic observatories at Lerwick (LER), ESK and Hartland (HAD) where geomagnetic measurements are continuously recorded. ESK is south of the Southern Uplands Fault (SUF; black dashed line) formed as a result of the closure of the Iapetus Ocean. Contains OS data © Crown copyright and database rights 2024.

and 2019 are selected to analyse the impact of season on the tipper estimates. Magnetic time-series from January of the year of interest plus November and December of the previous year are used to estimate the 'winter tipper', whereas those for May to July are used to compute the 'summer tipper'. Spring and autumn months are not considered because generally more energy is injected during geomagnetic storms around each equinox due to the increased coupling between the solar wind and magnetic field, known as the Russell-McPherron effect (Russell & McPherron 1973), whereas minimum geomagnetic activity occurs over the solstitial months. The cut-off

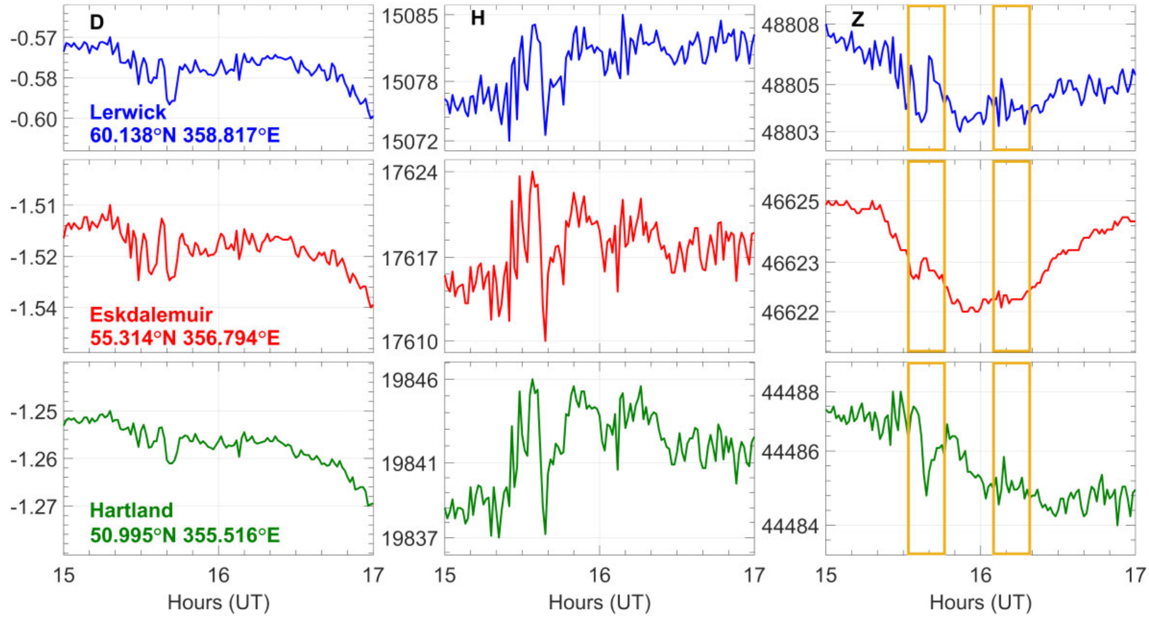

Figure 2. Two hour time-series of the magnetic declination (D, unit °E), horizontal intensity (H, unit nT) and the vertical intensity (Z, unit nT) measured at the three British geomagnetic observatories in Britain on 2021 January 24. The orange box highlights the dampened amplitude in Z at Eskdalemuir compared to the UK observatories to its north and south.

period is set at 10 240 s, as estimates at higher periods exhibit larger errors due to reduced data samples, leading to increased statistical uncertainty.

All tipper computations in this study are produced using KMSProMT data processing software developed by Smirnov (2003), which employs a repeated median algorithm by Siegel (1982). The advantage of Siegel's procedure is that the transfer function estimate remains stable even if up to 50 per cent of the input data are contaminated. In comparison, the least-squares procedure breaks down in the presence of outliers, such as steps or spikes in the measured data, making its solutions much more sensitive to their presence (Smirnov 2003). Therefore, algorithms used to estimate the tipper favour a robust statistical technique over the least-squares method.

The chosen processing configuration for KMSProMT uses the default value of 50 per cent overlap to improve statistical efficiency. The coherence threshold is set to 0.5; the maximum number of events in each data segment that shows coherence is set to 2000; decimation is fixed as 20 and the decimation factor is set to 1. To justify our choice of processing parameters, we compared our tipper estimates from data recorded at Niemegk Geomagnetic Observatory (NGK; 52.07 °N, 12.68 °E) between 2001 and 2017 with those of Ernst *et al.* (2020), who used the robust processing technique of Egbert & Booker (1986). Our results, shown in Fig. 3, are in close agreement with those of Ernst *et al.* (2020).

2.2 Establishing a stable tipper

Geomagnetic field variations are driven by different physical processes, each operating over distinct frequency ranges as illustrated in the amplitude spectrum produced by Constable & Constable (2004, 2023). Geomagnetic storms introduce fluctuating B_{ext} influences at higher frequencies, leading to large horizontal disturbances in B_{ext} that may deviate from the plane wave assumption. Estimating the tipper from long time-series using robust methods can minimize impacts of plane wave deviation (Egbert & Booker 1986). We aim to identify a tipper estimate at ESK that is least biased by deviations from the plane wave assumption, and refer to this as 'stable'. In order to establish the stable tipper estimate for ESK, we identify a tipper baseline that exhibits the least seasonal variation when compared to the average tipper value from 2001 to 2019 (particularly in relation to solar activity), relative to other years.

To evaluate the temporal stability of the tipper, we calculate percentage differences between the selected tipper estimates and the stable tipper.

We also calculate the tipper for each day using 1-s time-series in 2016 to prepare for source effect modelling and correction (see Section 2.3). These are based on the data for that day for periods in the range 170 to 683 s, and for three consecutive days in 2016 centred on the day of interest for longer periods, up to 2731 s.

2.3 An empirical model of the source effect

Previously, Vargas & Ritter (2016) modelled the temporal variations of the tipper at 11 mid-latitude geomagnetic observatories using a function with dependence on the day of the year (DOY) and a daily indicator of solar activity. They parametrized solar activity using daily values of $F10.7$ (estimated at 20:00 UTC), the 10.7 cm solar radio flux (Tapping 2013), corrected for changing Earth–Sun distance. Vargas & Ritter (2016) modelled temporal deviations from the 10-yr median tipper using data from 2003 to 2013. Their empirical model contained six independent coefficients:

$$\begin{aligned} T_{\text{source effect}}(\mathrm{DOY}, F10.7) = C_1 + C_2 \sin\left(\frac{2\pi \cdot \mathrm{DOY}}{N} + C_3\right) \\ + C_4 \cos\left(\frac{4\pi \cdot \mathrm{DOY}}{N} + C_5\right) \\ + C_6 \cdot F10.7 \end{aligned} \tag{2}$$

C_1 constitutes an offset. C_2 and C_4 represent the amplitude of annual and semi-annual seasonal variations, respectively; C_3 and C_5 are their respective phase values. C_6 accounts for the impact of space

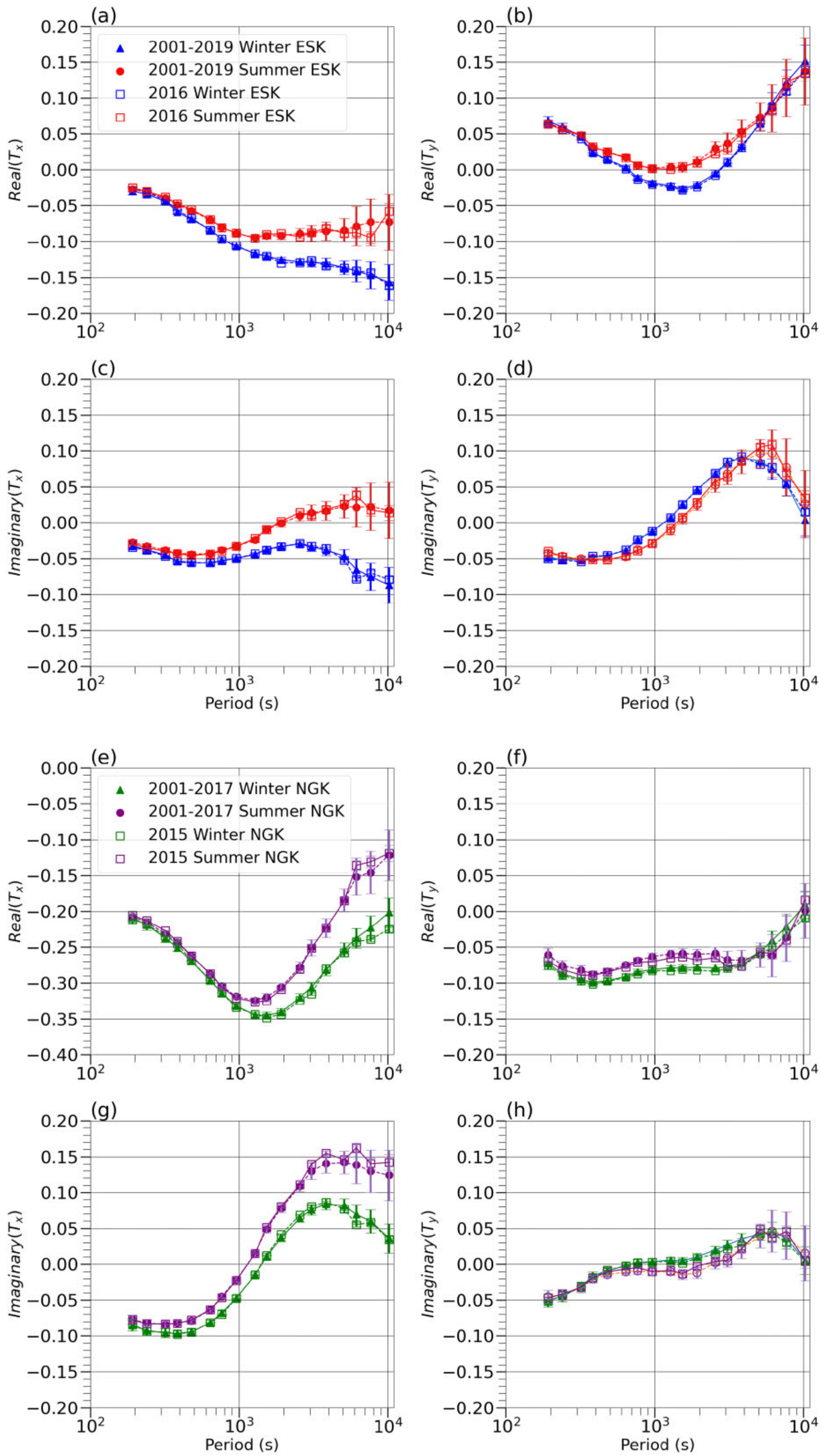

Figure 3. Seasonal variation in tipper estimates at ESK (panels a–d) and NGK (panels e–h). ESK tipper calculated for 2001–2019 separately for summer (red dots) and winter (blue triangles), results for 2016 are marked with open squares connected by dashed lines. NGK tipper calculated for 2001–2017 separately for summer (purple triangles) and winter (green dots) and for 2015 which are used to verify tipper processing parameters compared to those of Ernst *et al.* (2020) (marked with open squares). Panel (a) and (e) Re(T_x), (b) and (f) Re(T_y), (c) and (g) Im(T_x), (d) and (h) Im(T_y). Error bars are one standard deviation.

weather activity parametrized through $F10.7$. N is the total number of days in the year.

We applied this model to determine source effects at ESK using a linearized version of eq. (2) expressed as:

$$T_{\text{source effect}}(\text{DOY}, F10.7) = P_1 + P_2\cos\left(\frac{2\pi\cdot\text{DOY}}{N}\right) + P_3\sin\left(\frac{2\pi\cdot\text{DOY}}{N}\right) + P_4\cos\left(\frac{4\pi\cdot\text{DOY}}{N}\right) + P_5\sin\left(\frac{4\pi\cdot\text{DOY}}{N}\right) + P_6\cdot F10.7 \tag{3}$$

P_1 and P_6 are equivalent to C_1 and C_6 in eq. (2), whereas P_2 and P_3 (P_4 and P_5) are trigonometrically related to C_2 and C_3 (C_4 and C_5). We then find a least-squares solution to this set of equations, defining the daily tipper deviations for either T_x or T_y as:

$$\Delta T_i = T_i(t) - T_{\text{baseline}}(t), \tag{4}$$

where i is the day of the year in the tipper deviation (ΔT_i) from a stable baseline. Once the daily tipper at ESK has been obtained, we compute the tipper deviations using eq. (4). To prevent points with large errors from unduly affecting the solution, a least-squares fit to the data normalized by their standard deviations is also calculated. We refer to them as the normalized and the non-normalized solutions, respectively.

While $F10.7$ indicates solar activity, it does not characterize near-Earth impact of space weather disturbances on the magnetic field components. The daily definitive A_p index on the other hand is a proxy for the maximum daily global geomagnetic activity expressed in units of 2 nT (Mayaud 1980), calculated using the average of B_h measured at various, mainly Northern hemisphere, mid-latitude observatories (Mayaud 1980). It measures the degree of disturbance to the geomagnetic field, often associated with geomagnetic storm events (Lockwood *et al.* 2018). Therefore, we also investigated parametrizing the extent to which the geomagnetic field is disturbed in the empirical model of Vargas & Ritter (2016) using the A_p index instead of $F10.7$ so that eq. (2) is replaced by:

$$T_{\text{source effect}}(\text{DOY}, A_p) = C_1 + C_2\sin\left(\frac{2\pi\cdot\text{DOY}}{N} + C_3\right) + C_4\cos\left(\frac{4\pi\cdot\text{DOY}}{N} + C_5\right) + C_6\cdot A_p \tag{5}$$

From this model of $T_{\text{source effect}}$ for ΔT_i at ESK relative to the baseline, we correct the tipper at temporary MT sites near ESK for seasonal effects by adding ΔT_i corresponding to a specific DOY to the tipper estimated using $\widetilde{B}_x$ and $\widetilde{B}_y$ at nearby sites. Measurement durations at MT sites vary between 4 and 6 weeks, so the DOY is set to day of the median ΔT_i value within those weeks of recording at each site.

3 RESULTS

3.1 Temporal variation of the tipper at 3-month timescales

The mean summer and winter tipper estimates calculated using data from 2001 and 2019, and for 2016 and 2015, using 1-min time-series at ESK and NGK, respectively, are presented in Fig. 3. 2015 tipper is estimated for NGK in order to verify tipper processing parameters compared to those of Ernst *et al.* (2020). This reveals that large seasonal differences between the summer and winter tipper in Re(T_x), Im(T_x) occur at both ESK and NGK, increasing for periods longer than 640 s. The largest differences are seen in the longest periods, where winter tipper values are more than 200 per cent bigger than the summer values. For Re(T_y), the largest observed seasonal differences are found for periods of 600–3000 s, with decreasing differences for longer periods. For Im(T_y) the effect is less pronounced: the winter values rise slightly above the summer values at 5120 s period. Results for all components at both observatories shows a similar behaviour (Fig. 3). The geomagnetic latitude of NGK (51.87 °N) is significantly south of ESK (57.55 °N), but it appears that the two observatories are under similar levels of B_{ext} influence. This may imply that regional-scale source effects are superimposed onto the measured magnetic fields, resulting in the summer and winter tipper estimates from both observatories exhibiting systematic differences in their T_x components.

As seen in Figs 3(a)–(d), 2016 winter and summer tipper variations at ESK are compatible with the mean tipper for 2001–2019 at the majority of the periods, with the differences within their standard errors. Such relatively small tipper differences relative to 2001–2019 are not observed in the tipper of other years. Thus the 2016 summer and winter tippers show least seasonal variation compared to other years in solar cycles 23 and 24. The largest standard deviations are concentrated around the summer months at periods >3840 s, whereas those for the winter months are smaller. Ernst *et al.* (2020) showed that in winter, there are longer intervals where the plane wave assumption is fulfilled whereas the external B_z component is larger in the summer. Therefore, the 2016 winter tipper is chosen as the tipper baseline.

To visualize year-to-year changes in the tipper relative to this baseline, the summer and winter 2001–2019 tippers are displayed as percentage differences from the baseline values in Fig. 4. The winter differences (panels a–d) are smaller than the summer ones (panels e–h), again reflecting seasonal differences and the choice of baseline. Annual differences in winter Re(T_x) and Im(T_x) are significantly smaller overall than those of the T_y components. The deviations in summer Im(T_x) are much larger than those of Re(T_x). Across all years, the largest differences for Re(T_y) and Im(T_y) are consistently observed at intermediate periods (960–1536 s). However, the largest difference in winter Re(T_y) occurs at 640 s period (Fig. 4b) for which there is no obvious explanation.

3.2 Empirical model of the source effect at ESK

With these observations, we then attempt to find a model of seasonal dependence, following the approach of Vargas & Ritter (2016). Two sets of model coefficients are calculated for each of the two models described in Section 2.3 for 1 s data from 2016: one that parametrized source effects using $F10.7$ and the other using A_p, for both the non-normalized and normalized solutions. For the non-normalized solutions, both models fit the data better at lower periods as the root-mean-squared (RMS) misfit is larger at longer periods (>1000 s).

The different contributions of each term of the empirical source effect model given by eq. (3) to the prediction are plotted in Fig. 5 at 683 s period for Re(ΔT_y) in 2016. This period is chosen for illustration as it is within the range of periods most affected by geomagnetic storms in the UK (Campanyà *et al.* 2019).

The largest contribution to the model prediction (Fig. 5) is the annual variation. The lower amplitude semi-annual variation causes the two smaller peaks seen in the model prediction. Russell & McPherron (1973) proposed that semi-annual changes in

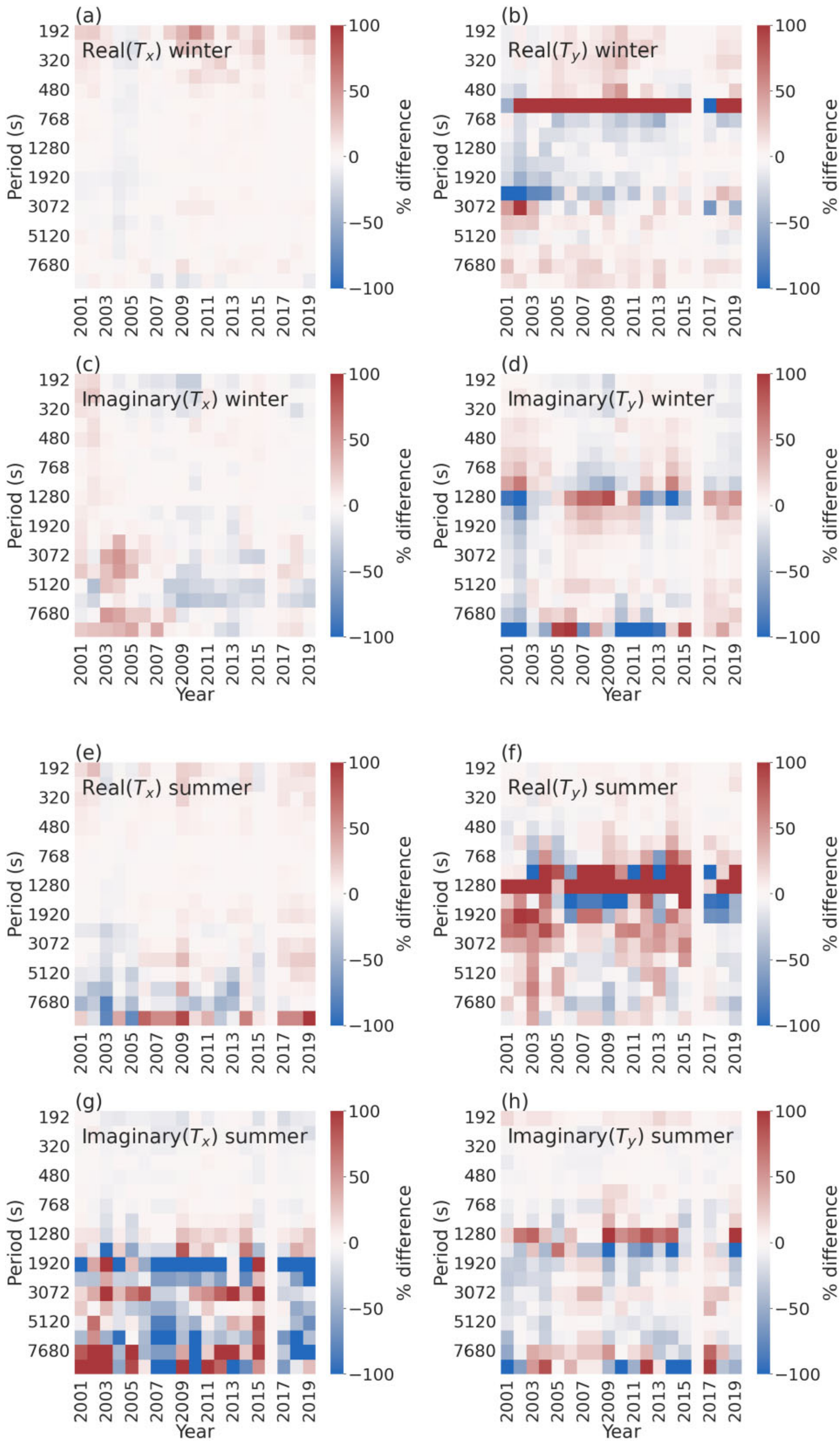

Figure 4. Yearly deviations from 2016 tipper baseline: Panels (a)–(d): relative differences calculated from winter time-series of 2001–2019 relative to those of winter 2016 for the Re(T_x), Re(T_y), Im(T_x) and Im(T_y). Panel (e)–(h): as for (a)–(d), but for summer time-series.

geomagnetic activity are a result of the semi-annual variation in the southward component of the interplanetary magnetic field. ΔT_i relative to either 2016 winter and 2016 summer results are reflected in the value of P_1 with other coefficients and their standard deviations and correlations unchanged.

$T_{\mathrm{source\ effect}}$ variations would have been smooth without the impact of the final terms in eqs (3) and (5). Short-term variations immediately after day 100 and around day 220 are visible in the $T_{\mathrm{source\ effect}}$ prediction, showing that solar activity strongly influences the model. Fig. 5 highlights the larger effect of using A_p instead of $F10.7$ to

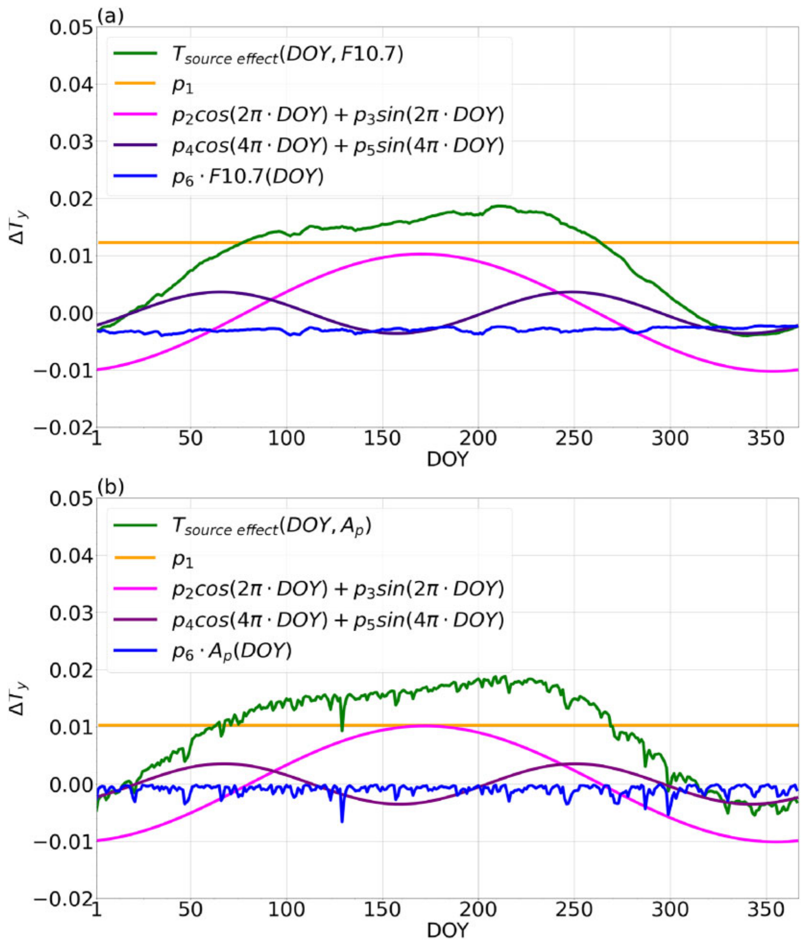

Figure 5. (a) Non-normalized solution of the Re(ΔT_y) source effect prediction (green) at 683 s period. The modelled annual contributions are shown in magenta, the semi-annual contributions in purple, the offset in red and the $F10.7$ in blue. Daily tipper deviations are relative to the 2016 winter baseline. (b) Same as (a), but using A_p to represent solar activity.

account for the impact of space weather. Note that with A_p, higher frequency variations are captured.

3.3 Comparison with other mid-to-high latitude observatories

To evaluate the impact of space weather-driven source effects and seasonal variations on tipper estimates, we modelled source effects at two additional mid-latitude observatories, Lycksele Magnetic Observatory (LYC) in northern Sweden and Chambon-la-Forêt Magnetic Observatory (CLF) in France, applying the same method as for ESK.

The C_2 values, representing the amplitude of the annual variation in eq. (2), at 512, 1024 and 2048 s computed for CLF, ESK and LYC are plotted as a function of geomagnetic latitude (rather than geographic latitude as chosen by Vargas & Ritter 2016) in Fig. 6 together with the C_2 coefficients derived for other mid-latitude observatories by Vargas & Ritter (2016) that were obtained by fitting deviations of daily estimates of T_x from the 10-yr median using 2003–2013 data for the same periods. Our non-normalized and normalized values are in close agreement to one another and within the error bars regardless of whether solar effects are parametrized by A_p or $F10.7$. The amplitudes of annual variations of $\Delta(T_x)$ increase with increasing geomagnetic latitude, and decrease with lower period (Fig. 6) in agreement with those of Vargas & Ritter (2016).

Fig. 6 shows that the standard deviations of the $F10.7$-based model C_2 coefficients are larger than those of the A_p-based model at all three periods. The standard deviations at ESK are also significantly smaller than those for CLF and LYC at each period. Re(ΔT_x) errors in CLF are extremely large, and its C_2 values do not fit the second-order polynomial curve of Vargas & Ritter (2016). The C_2 values of Re(ΔT_x) and Im(ΔT_x) from ESK deviate further from the second-order polynomial with increasing period, but not as much as CLF in Re(ΔT_x). Those for LYC deviate more than those of ESK from the polynomial fit. The second-order polynomial fit to the C_2 coefficients when plotted as a function of geomagnetic latitude is approximately symmetric about the geomagnetic equator in contrast to the fit as a function of geographic latitude (Fig. S6 in SI).

3.4 Discussion on the empirical model of the tipper variation at ESK

For all periods we have investigated, predictions of the normalized and non-normalized solutions of the tipper deviation with solar effects parametrized by A_p are a better fit to the data than those based on $F10.7$. Results for periods of 1024 and 2048 s for the

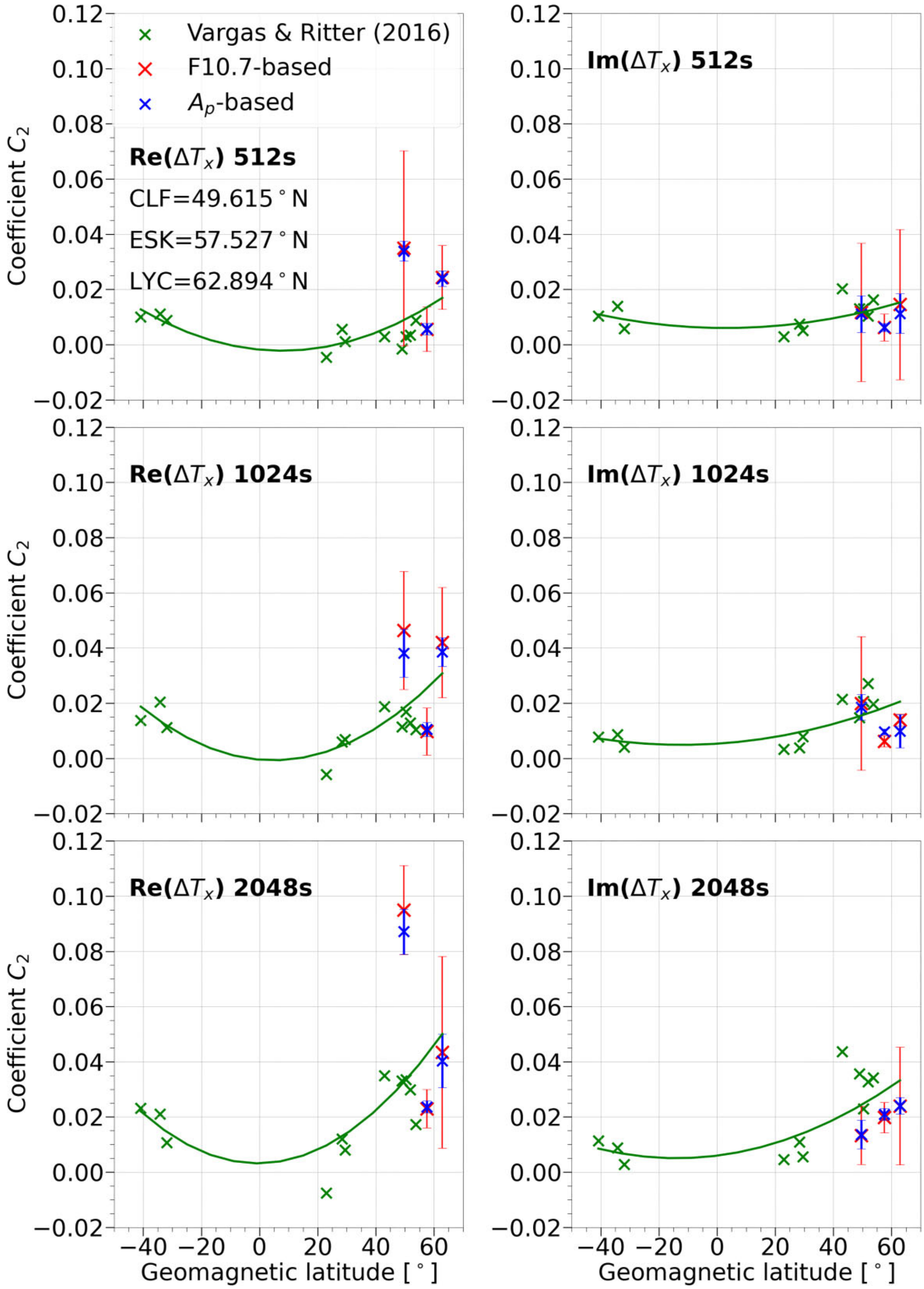

Figure 6. Dependence of coefficient C_2 (amplitude of annual variation) in the Re(ΔT_x) and Im(ΔT_x) components on geomagnetic latitude. Green crosses are values computed by Vargas & Ritter (2016); the green curve is the second-order polynomial fit as a function of geomagnetic latitude to their values. Red and blue crosses indicate the non-normalized C_2 values computed for source effect parametrized by $F10.7$ and A_p respectively for CLF, ESK and LYC. The error bars are propagated one standard deviation.

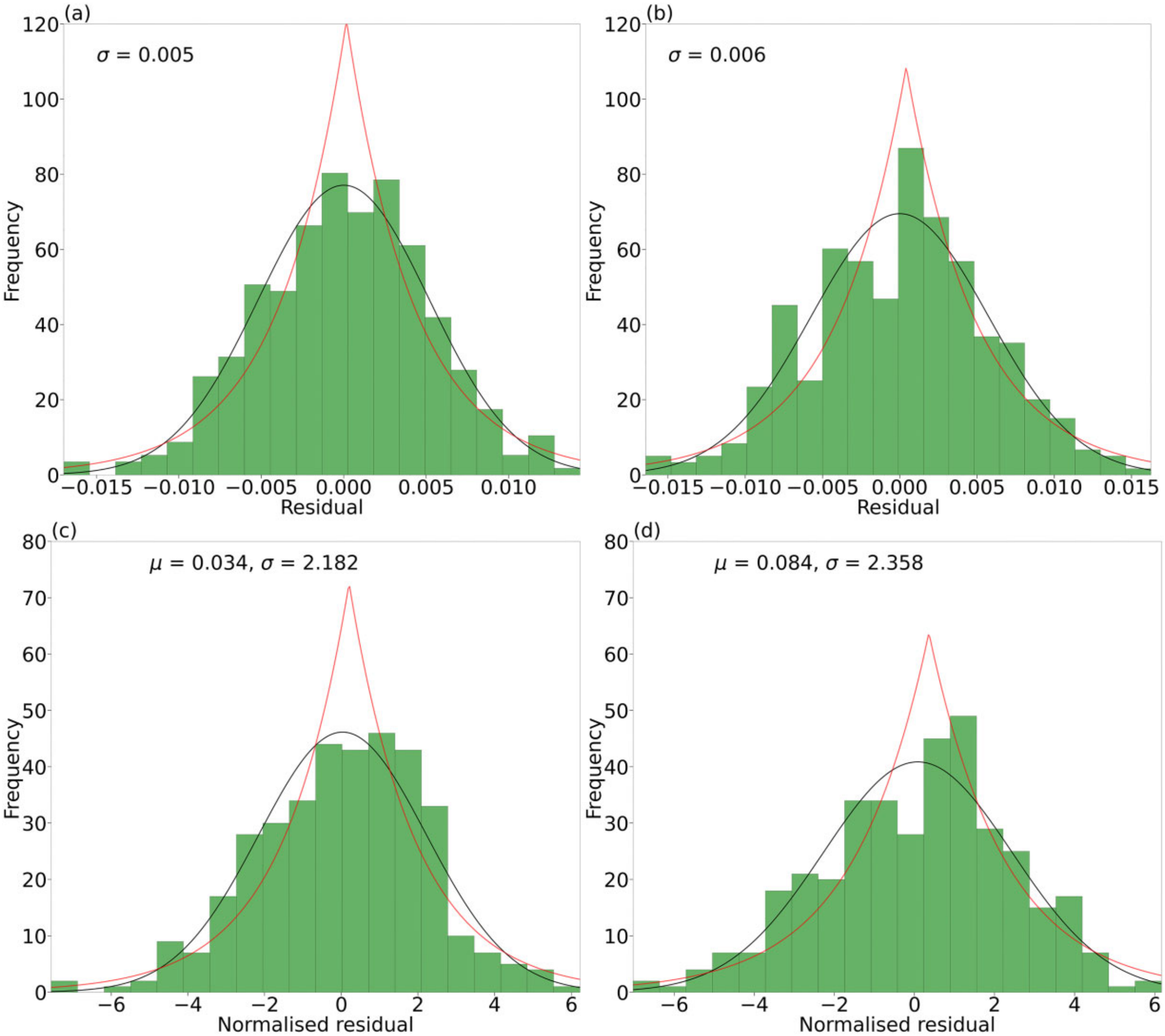

Figure 7. Histogram of residuals of the models of (a) Re(ΔT_x) and (b) Im(ΔT_x) and their best-fitting Gaussian (black) and Laplacian (red) distribution at 683 s period when their solar effect is parametrized by A_p. (c) and (d) are the equivalents for the normalized model. μ is the mean residual and σ is the standard error of the Gaussian fit.

$F10.7$-based and A_p-based models are presented in Fig. S7–Fig. S11 in the SI. The statistics of the RMS misfit at these periods, and at 512 and 683 s, are listed in Table S2 in the SI. Coefficients of the A_p model have lower correlations than those of the $F10.7$-based model (Fig. S5 in SI). P_1 and P_6 are anticorrelated. This suggests that A_p is a better choice to parameterize source effects.

Figs 7(a) and (b) show histograms of the real and imaginary ΔT_x residuals at 683 s for the non-normalized solution. Both distributions exhibit a strong peak at zero and are broadly symmetrical, showing low skew. The gradients around their peaks are steep and far from an ideal Gaussian distribution. However, the histograms are a worse fit to a Laplacian distribution (Fig. 7). The residuals for the normalized solution for the same components are shown in Figs 7(c) and (d), respectively. Again the mean normalized residual values peak at zero but the standard deviations are significantly greater than one. This demonstrates that the model captures the large-scale features of the data, but there is considerable un-modelled signal.

The source effect predictions relative to the baseline with solar activity parametrized by A_p at a period of 683 s are shown in Fig. 8. We find that the non-normalized solution captures the daily variations of ΔT_i better than the normalized solution. The prediction deviates most from the signals around days 30, 80, 220 and 260 when solar activity is highest. Re(ΔT_x) and Re(ΔT_y) reach their maximum around the middle of 2016 and this is captured in the predictions. We observe a decrease in annual and semi-annual seasonal variations during the fourth quarter of 2016, accompanied by a decrease in the real component tipper deviations by 0.02 relative to their peak values (Fig. 8). Im(ΔT_y) also has a larger semi-annual variation.

Daily tipper deviations are smaller at shorter periods than at longer periods (Fig. S10 and Fig. S11 in SI), which suggests a larger source field influence at periods longer than 683 s. The influence of solar activity appears to be subtle at <1000 s periods — the C_6 coefficient is an order of magnitude smaller than at longer periods. At 2048 s, the predictions of the normalized and non-normalized solutions show greater absolute differences from each other than at lower periods.

We compare how seasonal effects impact the value of the C_2 coefficient at the mid-latitude observatory NGK, obtained by Vargas & Ritter (2016), with those of ESK for real and imaginary ΔT_x. At periods of 1024 s and above, the predictions of tipper deviations derived for both observatories show a seasonal peak during the summer months followed by a gradual decline in the autumn months before stabilizing during the last 40 days of the year.

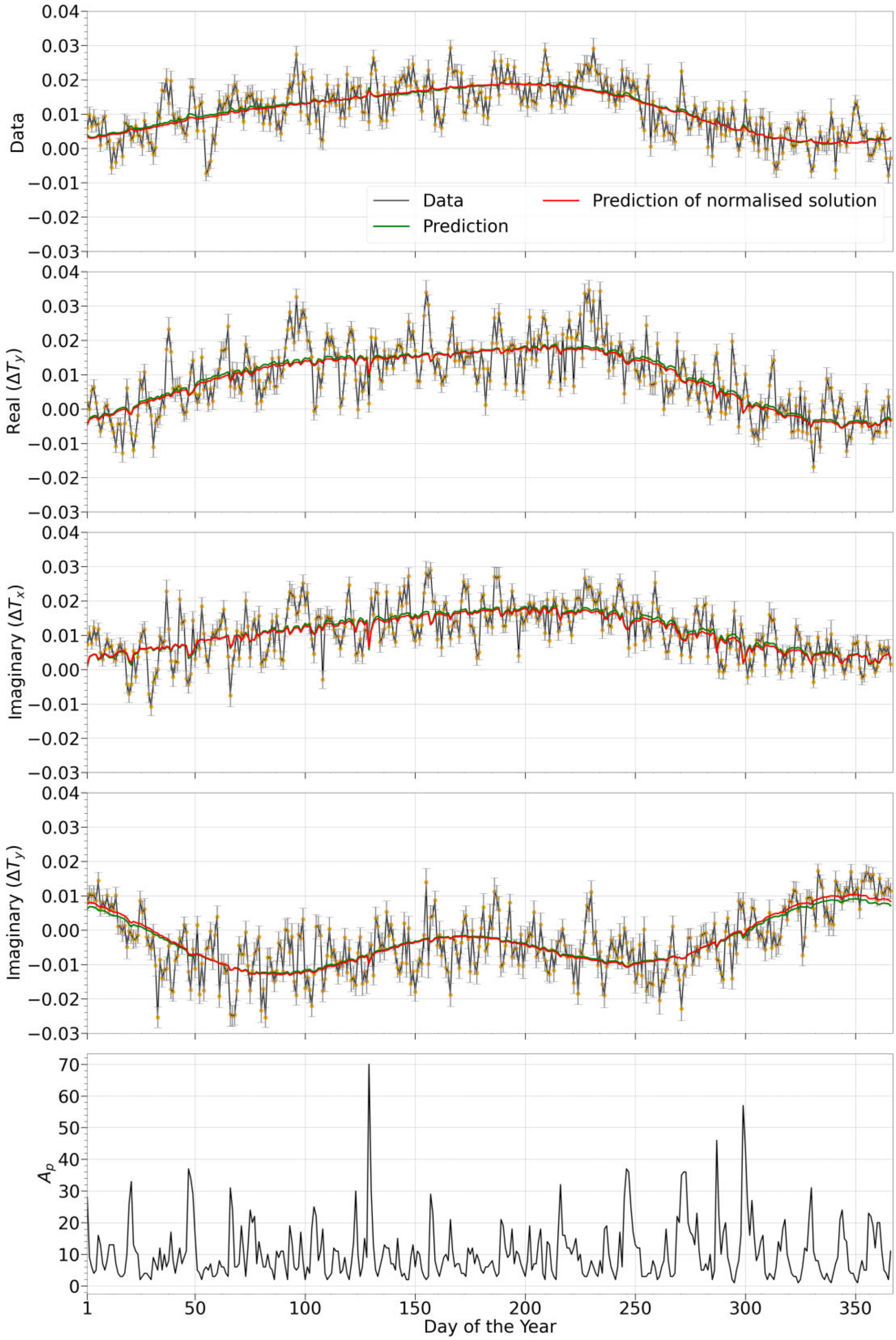

Figure 8. Predictions of the tipper variation in 2016 at ESK by normalized and non-normalized solutions at 683 s, where source effect is parametrized by the A_p index. Daily tipper deviations are the orange dots and their propagated one standard deviation are represented by the grey error bars. The green curves represent the non-normalized $T_{\mathrm{source\ effect}}$ solution and the red curves the normalized solution.

To test whether tipper temporal variations also show correlation with long-term solar activity at ESK, daily tipper estimates for 2016–2019 are shown in Fig. 9 together with non-normalized and normalized models fits to them with solar activity parametrized by A_p. From Fig. 9, we see a strong annual seasonal dominance in the temporal variability, with a maximum around June over consecutive years in Re(ΔT_x), Re(ΔT_y) and Im(ΔT_x) components, and a minimum in Im(ΔT_y). In contrast to other components, Im(ΔT_y)

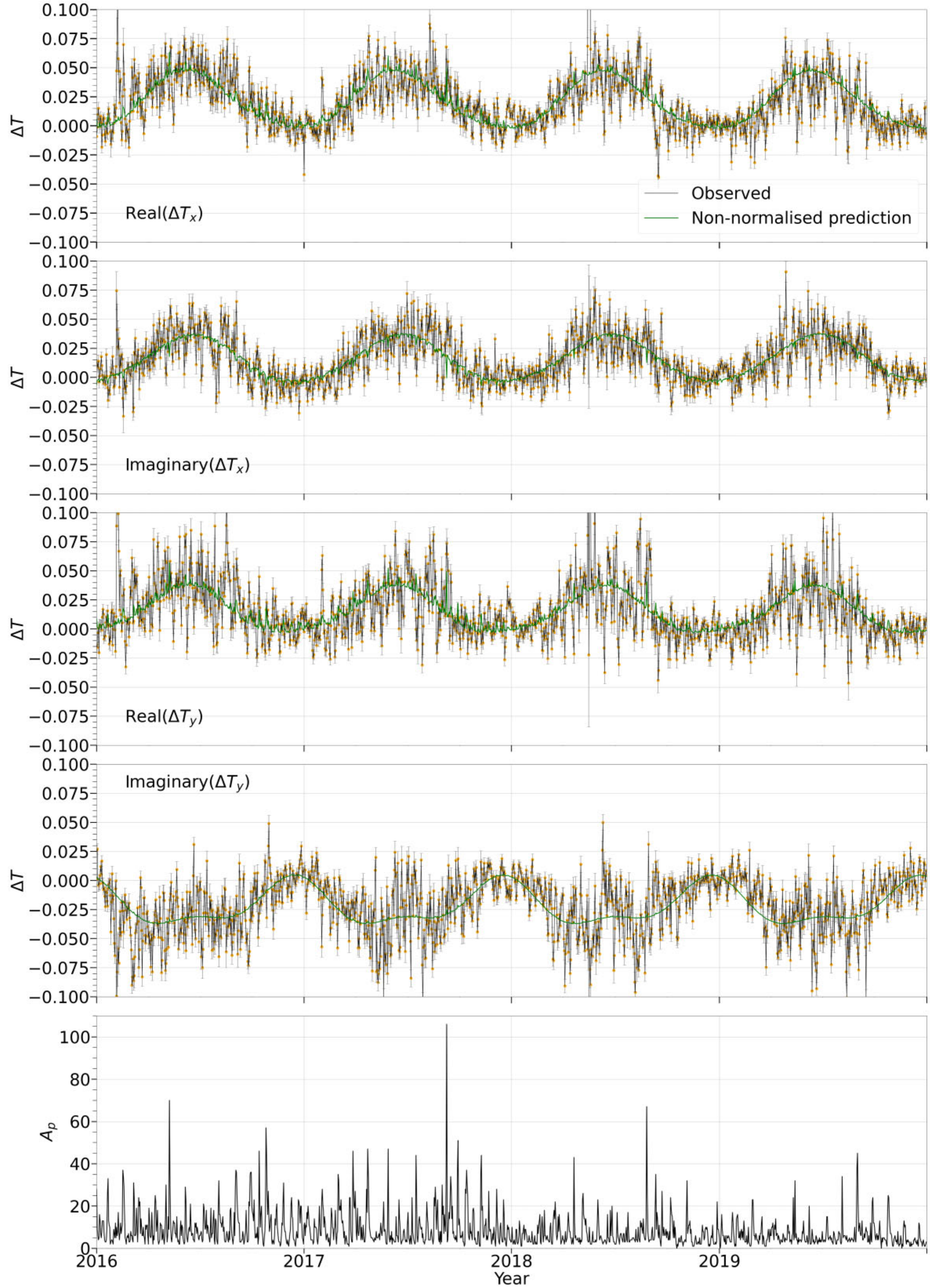

Figure 9. Predictions of the tipper variation in 2016-2019 at ESK by normalized and non-normalized solutions at 2048 s. The four upper panels show deviations of the four tipper components relative to the 2016 winter tipper baseline, and the bottom panel shows the A_p index. Non-normalized predictions in green are fitted to tipper deviations represented by the orange dots. The grey error bars are one standard deviation.

increases after day 280 because of the phase of its annual component. The periodical seasonal variation is more pronounced at longer periods, such as the 2048 s period shown in Fig. 9, than at shorter (<1000 s) periods (Fig. S7–S11 in SI). These patterns in the seasonal variation of the tipper at 2048 s period were also observed by Vargas & Ritter (2016) in their analysis of the variability of the

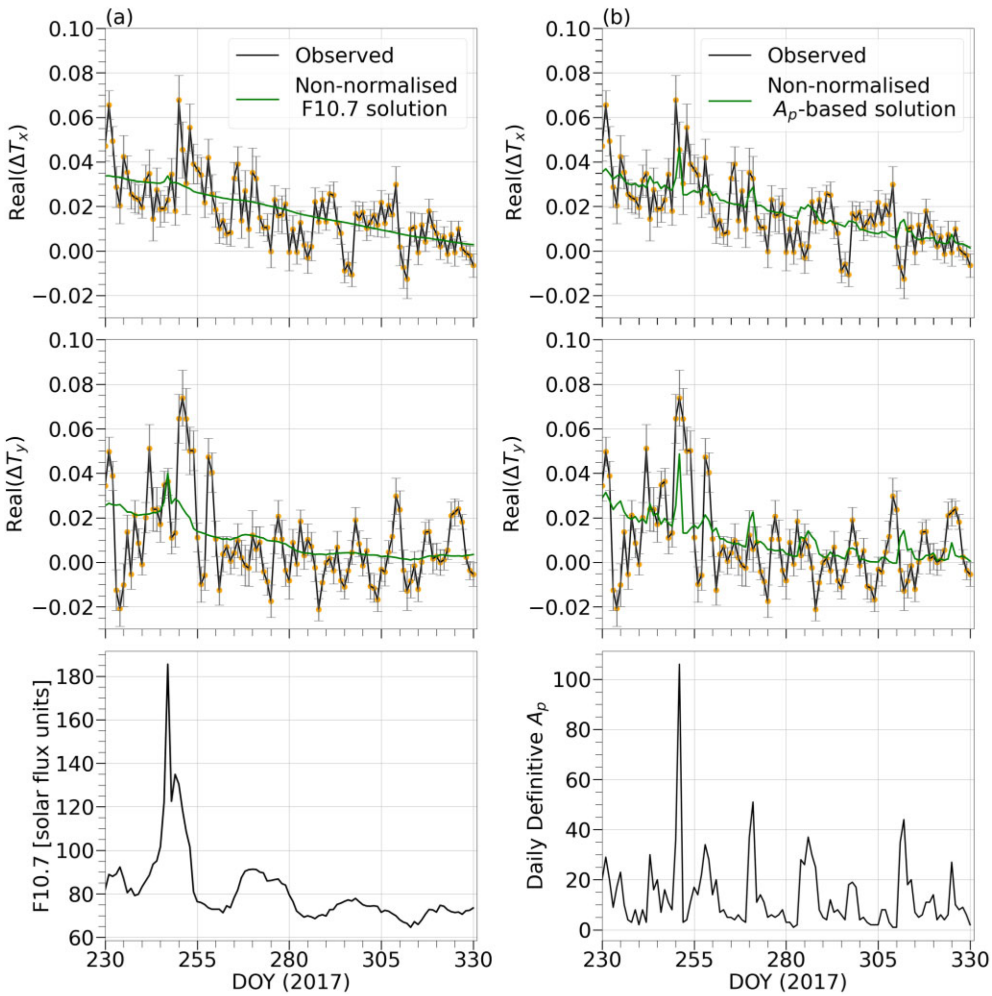

Figure 10. Impact of source effect on the Re(ΔT_x) and Re(ΔT_y) components. (a) Non-normalized solutions in green fitted to the 2017 tipper deviations plotted as orange dots at ESK for 2048 s period using daily $F10.7$ in the model. The grey error bars are one standard deviation. (b) Same as (a) but with the solution computed using the daily A_p index in place of the $F10.7$ index.

daily tipper estimates over consecutive years at other mid-latitude magnetic observatories.

A clear example of space weather-dependent 'source effects' present in the longer period tipper estimates for mid-latitude observatories is shown in Fig. 10 for the September 2017 geomagnetic storm, where the storm occurs on days 249 to 253. Fig. 10(a) shows the non-normalized prediction at 2048 s period in Re(ΔT_x) and Re(ΔT_y) components with a dependence on the $F10.7$ index. The model predicts a smoothed variation and matches poorly with the data whereas the predictions of the non-normalized solution from eq. (5) with dependence on the daily A_p shown in Fig. 10(b) are in slightly better agreement with the data. This example demonstrates the importance of accounting for the influence of solar activity during geomagnetic storm conditions. However, as both $F10.7$ and A_p indices are daily values, neither model is able to capture the higher frequency variations (hourly) in the tipper deviation.

4 APPLYING SEASONAL CORRECTION TO LONG-PERIOD MT DATA

Accounting for seasonal effects in tipper estimates should result in more accurate modelling of the subsurface conductivity. In order to investigate the efficacy of this approach, we chose the predictions of the non-normalized A_p-based model relative to the baseline for seasonal effect correction of LMT data collected around ESK (Fig. S12 in SI). This model presented a better fit to the data with lower parameter correlation than that of the $F10.7$-based model. However, for most periods the corrections are not dependent on the way solar activity is parametrized or whether the solution is normalized.

To assess period-dependent variations in tipper corrections, we analysed data from four LMT sites within 80 km of ESK (NT15, NT66, NY69 and NY73, Hübert *et al.* 2025). These magnetic data were recorded in 2022 as part of the UK NERC-funded Space Weather Instrumentation, Measurement, Modelling and Risk (SWIMMR) Activities in Ground Effects project, aimed at substantially improving existing geoelectric field modelling capability by making new tipper and LMT measurements in the British Isles to supplement existing MT data (Hübert *et al.* 2022). Corrections derived for a particular period at ESK would only be appropriate for nearby sites, where 'nearby' is dependent on the period since shorter period signals do not penetrate as far into the ground, as well as the exact details of the subsurface conductivity structure. Hence there is not an exact limit to the radius over which seasonal corrections to the tipper can be made.

Correction values to account for seasonal effects as a function of period are plotted in Fig. 11 for each tipper component at four LMT

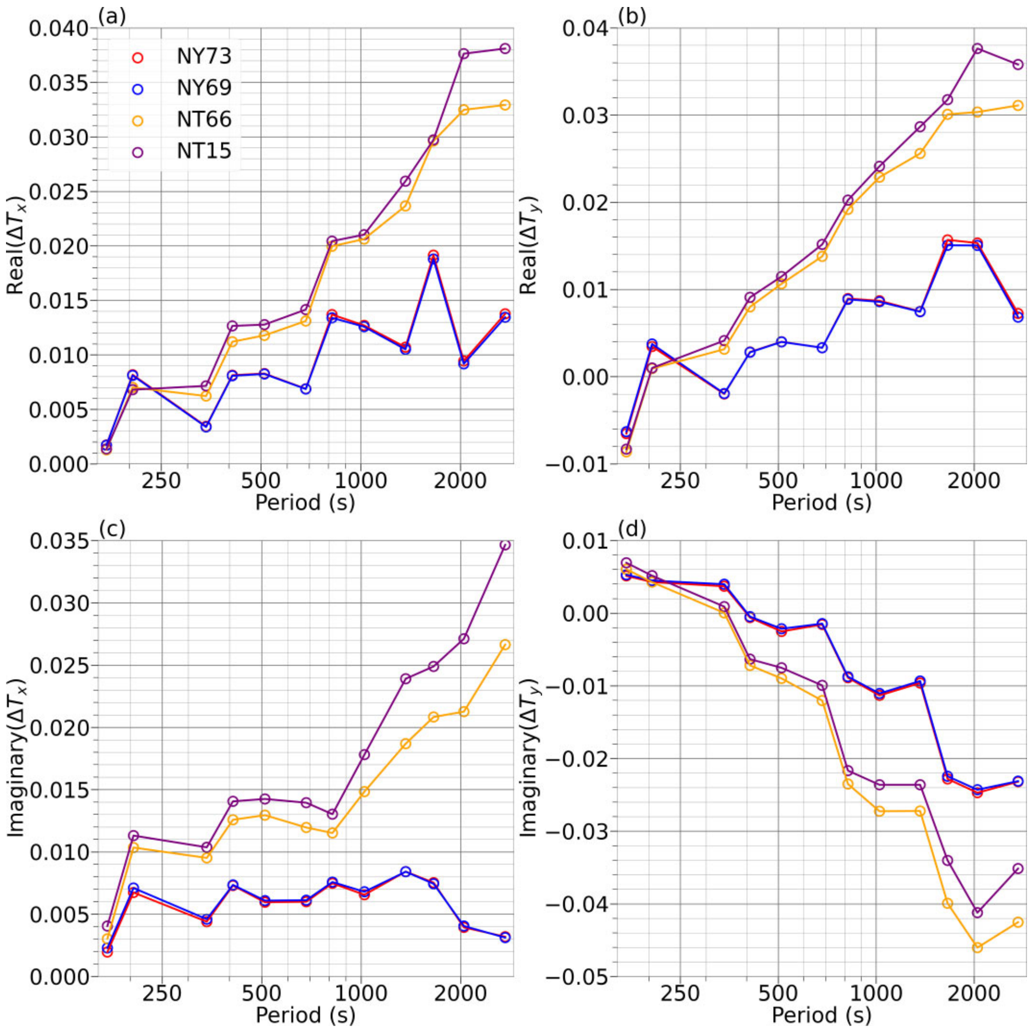

Figure 11. Values to correct for the seasonal effect based on prediction from the non-normalized A_p-based model relative to the baseline as a function of periods from 170 s to 2731 s at LMT sites close to ESK (see Fig. 12) for (a) Re(ΔT_x), (b) Re(ΔT_y), (c) Im(ΔT_x) and (d) Im(ΔT_y).

sites. Tipper correction at each period is taken from the median tipper deviation derived from the non-normalized A_p-based model at ESK relative to the baseline for each day per site (an example at 2048 s period is shown by the red arrow in Fig. S12 in the SI). We observe that the corrections for these sites are similar at the shortest periods. For periods longer than 512 s, there is an increase in the magnitude of the correction in all components and there the correction peaks at 1638 s for the Re(ΔT_x) components at NT66 and NT15. Fig. 11 also shows that corrections for NT15 and NT66 diverge from those of NY69 and NY73 with increasing period for all components. The corrections to Im(ΔT_y) are increasingly negative with increasing period until they become less negative after 2048 s.

The tipper is often visualized as induction arrows to better understand the direction and strength of B_{ind}. Following the Parkinson convention, these arrows point towards areas of higher electrical conductivity (Parkinson 1959; Lilley & Arora 1982). The length of each induction arrow provides an indication of the magnitude of the subsurface conductivity contrast. Fig. 12 show induction arrows, at NT15, NT66, NY69 and NY73 before and after correction at 2048 s period. In Fig. 12(a), orientations of the real induction arrows before correction show greater differences from the corrected arrows at NT15 and NT66 than those of NY69 and NY73. This is because the real parts of the tipper deviations become larger towards the summer as shown in Fig. 8 and Fig. S12 in the SI, and NT15 and NT66 data were collected between day 73 and day 119. The corrected proposed induction arrows at each site are not significantly different in magnitude and direction from the uncorrected: the magnitude of the difference between the uncorrected and corrected arrows are in the range of 0.01–0.03 for the real part and 0.02–0.05 for the imaginary part. Bearing in mind that interpretations of subsurface conductivity structure based on the tipper produced using weeks of measured magnetic field data can be biased by seasonal effects caused by increased geomagnetic activity (Sanaka & Neska 2023), using a parameter representing solar activity at higher fidelity in the seasonal effect model might improve the corrections at periods of interest for GDS and MT studies.

5 CONCLUSIONS

Modern geomagnetic field data measured at ESK observatory reveal significantly dampened B_z component variations for periods less than an hour relative to those at other nearby sites, confirming past observations. The measured magnetic field variations consist of a contribution from the inducing B_{ext} variations in the ionosphere and magnetosphere, and an internal contribution that is driven by

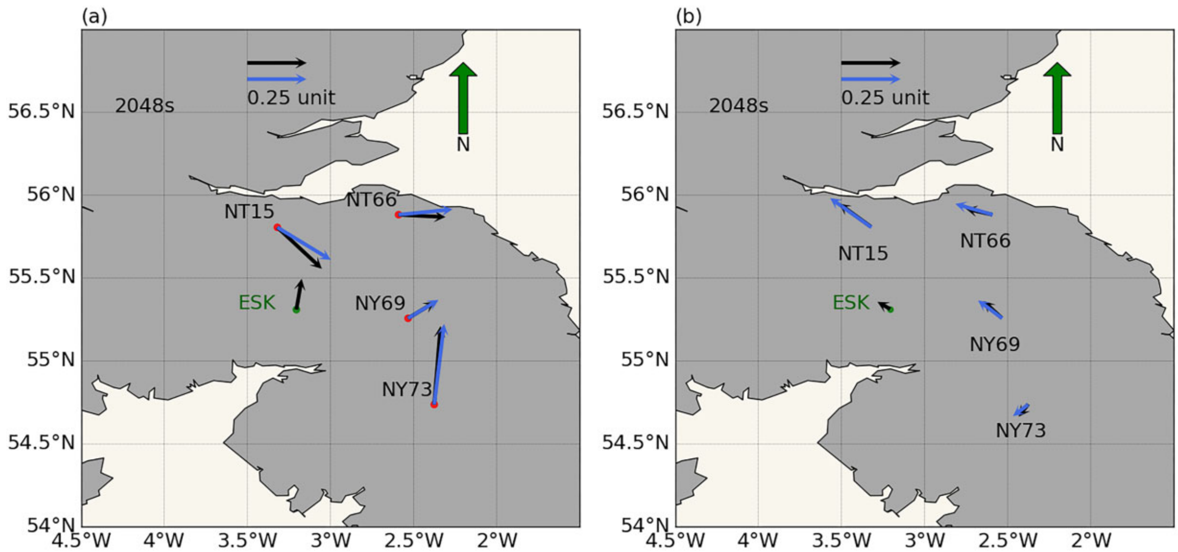

Figure 12. (a) Original real induction arrows (black) and corrected real induction arrows (blue) point at ESK (green dot) and nearby LMT sites (red dots) for 2048 s period after Parkinson convention (pointing towards areas of higher electrical conductivity). (b) Same as (a), but for original (black) and corrected (blue) imaginary induction arrows.

electrical currents induced by changes in B_{ext}. Working under this assumption, past studies of the Eskdalemuir anomaly have not considered the effect of seasonal source changes. Our study identified the presence of source effects on $B_{z,\text{ind}}$ at mid-latitudes in the derived tipper estimates. This confirms conclusions of Beamish (1981) that the tipper is increasingly affected by source effects at mid-latitudes with increasing period.

We show that seasonal effects in the tipper derived from 1-min geomagnetic data for the three summer months of 2001–2019 differ from estimates based on data from the three winter months, especially for periods longer than 1000 s. Summer and winter tippers for 2016 show the least seasonal variations relative to the 2001–2019 summer and winter tippers. The tipper estimated from the three winter months data are likely to approximate better the plane wave assumption because data recorded during winter are less disturbed by the ionospheric current system than in the summer.

Subsequently, 1-s magnetic time-series are used to compute tipper deviations relative to the 2016 winter values, referred to as the baseline. In order to model the temporal deviation of daily tipper throughout the year, we use an empirical model consisting of annual and semi-annual terms and along with a term dependent on solar activity (Vargas & Ritter 2016). The normalized RMS difference between the data and model prediction is >2 at 683 s for all four components of the tipper deviation, and is similar at longer periods. This indicates that the model does not reflect the full variability of the data. However, the residuals are approximately normally distributed with zero mean, and this relatively simple model captures much of the systematic variability, also seen from data predictions in Fig. 8 and Fig. 9. It might be improved if the source effect was parametrized more finely in time so higher frequency variations are captured whilst still accounting for the annual and semi-annual signals. It would be worth investigating whether a better fit could be obtained using a parameter characterizing source effects with values available more than once a day.

Encouragingly, the model follows the general trend of the observed data at ESK, matching a strong annual signal in all components of the tipper deviation at all periods, with a significant semi-annual signal in $\mathrm{Im}(\Delta T_y)$. For periods >1000 s, the impact of source effects is seen in the prediction, and the model in which solar activity is parametrized by the A_p index captured more of the variability in the tipper deviation during geomagnetic storms than when $F10.7$ is used. This dependence is also demonstrated by tipper deviations over consecutive years (2016–2019) used as input data for the empirical model. The same method is used to study tipper deviations from CLF and LYC observatories, as well as the 11 other mid-latitude observatories used in Vargas & Ritter's (2016) study, which all showed similar seasonal variability.

The empirical model fit indicates times of the year when deviations from the plane wave assumption impact the tipper at mid-latitudes. We observe an increase in the tipper deviation as a function of period >512 s for all components. This has implications for MT fieldwork, where the measurement duration is limited to several weeks per site. The results were used to correct each component of the tipper relative to the baseline at four locations (<80 km from ESK) where MT data were collected in 2021–2022. The corrected tipper at each site does not differ greatly in magnitude and direction from the uncorrected tipper and for inversion modelling are within assumed modelling errors. This suggests that revisions to past interpretations of the ground conductivity beneath Eskdalemuir owing to seasonal effects are not required.

ACKNOWLEDGMENTS

The results presented in this paper are based on parts of Guanren Wang's University of Edinburgh Master's thesis. We relied on data collected at Eskdalemuir, Niemegk, and other observatories. We thank GFZ Potsdam, the Geological Survey of Sweden and Institut de Physique du Globe de Paris for supporting their operation and INTERMAGNET for promoting high standards of magnetic observatory practice. We thank Maxim Smirnov of Luleå University of Technology for developing the KMSPro Magnetotelluric Data Processing software.

The authors thank Jaime Araya Vargas for providing us with C_2 values of the 11 mid-latitude observatories obtained by Vargas & Ritter (2016). We also thank editor Dr Ute Weckmann and all reviewers for their comments that helped us improve the quality of the manuscript.

This work was funded by the Jane Plant Fellowship Scheme for Further Education Support of the British Geological Survey and also funded under UK Natural Environment Research Council (NERC) Grant NE/V002694/1 'SWIMMR Activities in Ground Effects (SAGE)'. This paper is published with the permission of the Executive Director of the British Geological Survey (UKRI).

SUPPORTING INFORMATION

Supplementary data are available at *GJIRAS* online.

suppl_data

Please note: Oxford University Press is not responsible for the content or functionality of any supporting materials supplied by the authors. Any queries (other than missing material) should be directed to the corresponding author for the paper.

DATA AVAILABILITY

All 1-s provisional data and 1-min definitive data are freely available. ESK and LYC data can be downloaded from INTERMAGNET (https://intermagnet.github.io/). The International Real-time Magnetic Observatory Network is a worldwide magnetic data exchange centre amongst participating organisations using satellite and internet connection. CLF data are downloaded from http://www.bcmt.fr/DATABANK/DEFINITIVE/clf/. Daily $F10.7$ values are provided by Natural Resources Canada and they are downloaded from https://spaceweather.gc.ca/forecast-prevision/solar-solaire/solarflux/sx-5-en.php. Daily A_p index is provided by the British Geological Survey (UKRI), downloaded from https://geomag.bgs.ac.uk/data_service/data/magnetic_indices/apindex.html. Geomagnetic dipole coordinates of observatories are calculated for 13th generation of the International Geomagnetic Reference Field, available at https://geomag.bgs.ac.uk/data_service/models_compass/coord_calc.html. The SWIMMR Activities in Ground Effects MT data are deposited in the NERC Geoscience Data Centre (NGDC) and openly accessible on https://webapps.bgs.ac.uk/services/ngdc/accessions/index.html#item187579.

REFERENCES

Anusha, E. & Arora, K., 2023. Annual/seasonal variation in induction vectors at different geological locations in an Indian Sector, *Pure appl. Geophys.,* **180,** 3527–3543.

Arora, B.R., Trivedi, N.B., Vitorello, I., Padilha, A.L., Rigoti, A. & Chamalaun, F.H., 1999. Overview of Geomagnetic depth soundings (GDS) as applied in the Parnaíba Basin, northeast Brazil, *Rev. Bras. Geof.,* **17,** 43–65.

Bailey, R.C. & Edwards, R.N., 1976. The effect of source field polarization on geomagnetic variation anomalies in the British Isles, *Geophys. J. R. astr. Soc.,* **45,** 97–104.

Baker, D.N., 1998. What is Space Weather?, *Adv. Space Res.,* **22,** 7–16.

Beamish, D., 1979. Source field effects on transfer functions at mid-latitudes, *Geophys. J. R. astr. Soc.,* **58,** 117–134.

Beedle, J.M., Rura, C.E., Simpson, D.G., Cohen, H.I., Moraes Filho, V.P. & Uritsky, V.M., 2022. A User's guide to the magnetically connected space weather system: a brief review, *Front. Astron. Space Sci.,* **8,** 1–24.

Beggan, C.D., Clarke, E., Lawrence, E., Eaton, E., Williamson, J., Matsumoto, K. & Hayakawa, H., 2024. Digitized Continuous Magnetic Recordings for the August/September 1859 Storms From London, UK, *Space Weather,* **22**(3), e2023SW003807. doi:10.1029/2023SW003807.

Campanyà, J., Gallagher, P.T, Blake, S.P., Gibbs, M., Jackson, D., Beggan, C.D., Richardson, G.S. & Hogg, C., 2019. Modeling geoelectric fields in Ireland and the UK for space weather application, *Space Weather,* **17**(2), 216–237.

Chamalaun, F.H., 1985. Geomagnetic deep sounding experiment in the central Flinders Ranges of South Australia, *Phys. Earth planet. Inter.,* **37,** 174–182.

Clarke, E., Baillie, O., Reay, S.J. & Turbitt, C.W., 2013. A method for the near real-time production of quasi-definitive magnetic observatory data, *Phys. Earth planet. Inter.,* **65,** 1363–1374.

Constable, C.G. & Constable, C.C., 2004. Satellite Magnetic Field Measurements: Applications in Studying the Deep Earth, *Geophys. Monogr. Ser.,* pp. 146–160, AGU Publications.

Constable, C.G. & Constable, C.C., 2023. A grand spectrum of the geomagnetic field, *Phys. Earth planet. Inter.,* **344,** 107091. doi:10.1016/j.pepi.2023.107090

Edwards, R.N., Law, L.K. & White, A., 1971. Geomagnetic variations in the British Isles and their relation to electrical currents in the ocean and shallow seas, *Phil. Trans. R. Soc.,* **270,** 289–323.

Egbert, G.D. & Booker, J.R., 1986. Robust estimation of geomagnetic transfer functions, *Geophys. J. R. astr. Soc.,* **87,** 173–194.

Ernst, T., K., Nowożyński & Jóźwiak, W., 2020. The reduction of source effect for reliable estimation of geomagnetic transfer functions., *Geophys. J Int.,* **221,** 415–430.

Honkura, Y., 1978. Electrical conductivity anomalies in the Earth, *Surv. Geophys.,* **3,** 225–253.

Hübert, J., Eaton, E., Beggan, C.D. & Thomson, A.W.P., 2022. *Developing a UK new ground electric field model for SWIMMR N4 (SAGE): Interim Report,* pp. 43 (OR/22/067), British Geological Survey.

Hübert, J., Eaton, E., Beggan, C.D., Collins, A. & Wang, G., 2025. Long-period Magnetotelluric data collected at 44 sites in Scotland, England and Wales. NERC EDS National Geoscience Data Centre. (Dataset). https://doi.org/10.5285/14274b67-86a5-4d9d-b3f4-20c6d20228d7

Hutton, V.R., Sik, J.M. & Gough, D.I., 1977. Electrical conductivity and tectonics of Scotland, *Nature,* **13,** 617–620.

Jain, S. & Wilson, C.D., 1967. Magneto-Telluric Investigations in the Irish Sea and Southern Scotland, *Geophys. J. R. astr. Soc.,* **12,** 165–180.

Jones, A.G. & Hutton, R., 1977. Magnetotelluric Investigations of the Eskdalemuir Anomaly S. Scotland Preliminary Results, *Acta Geodaet., Geophys. et Montanist. Acad. Sci. Hung. Tomus.,* **12,** 111–115.

Jones, A.G. & Hutton, R., 1979. A multi-station magnetotelluric study in southern Scotland - I. Fieldwork, data analysis and results, *Geophys. J. R. astr. Soc.,* **56,** 329–349.

Lilley, F.E. & Arora, B.R., 1982. The sign convention for quadrature Parkinson arrows in geomagnetic induction studies, *Rev. Geophys.,* **20,** 513–518.

Lockwood, M., Owens, M.J., Barnard, L.A., Scott, C.J., Watt, C.E. & Bentley, S., 2018. Space climate and space weather over the past 400 years: 2. Proxy indicators of geomagnetic storm and substorm occurrence, *J. Space Weather Space Clim.,* **8,** A12. doi:10.1051/swsc/2017048

Maksymchuk, V., Chobotok, I., Klymkovych, T., Kuderavets, R., Nakalov, E. & Otruba, Y., 2018. Complex Magnetovariational and Tectonomagnetic Monitoring of Recent Geodynamics in the Western Slope of the Antarctic Peninsula, *Ukrainian Antarctic J.,* **1(17),** 3–19.

Mayaud, P.N., 1980. Derivation, Meaning, and Use of Geomagnetic Indices, *Geophys. Monogr. Ser.,* **22,** 40–85 . American Geophysical Union, Washington, D. C.

Oliver, G., Stone, P. & Bluck, B., 2002. The Ballantrae Complex and Southern Uplands terrane, in *The Geology of Scotland,* 4th edn, pp. 167–200, ed. Trewin, N.H., The Geological Society.

Osemeikhian, J.E.A. & Everett, J.E., 1968. Anomalous Magnetic Variations in Southwestern Scotland, *Geophys. J. R. astr. Soc.,* **15,** 361–366.

Parkinson, W.D., 1959. Directions of Rapid Geomagnetic Fluctuations, *Geophys. J. R. astr. Soc.,* **2,** 1–14.

Parkinson, W.D. & Jones, W.F., 1979. The Geomagnetic Coast Effect, *Rev. Geophys.,* **17,** 1999–2015.

Rokityansky, I.I., Klymkovych, T.A., Babak, V.I. & Isac, A., 2012. Annual and diurnal variations of induction vectors in relation to geodynamic processes, *Geomatics, Nat. Hazards Risk.,* **3,** 239–249.

Russell, C.T. & McPherron, R.L., 1973. Semiannual variation of geomagnetic activity., *J. geophys. Res.,* **78,** 92–108.

Sanaka, S. & Neska, A., 2023. Temporal stability of induction vectors from Antarctic Peninsula, AIA INTERMAGNET observatory, AIA INTERMAGNET observatory, *Ukrainian Antarctic J.,* **21**(26), 3–12.

Schmucker, U., 1969. Conductivity anomalies, with special reference to the Andes, in *The Application of Modern Physics to the Earth and Planetary Interiors,* pp. 125–138, ed. Runcorn, S.K., Wiley-Interscience.

Siegel, A.F., 1982. Robust regression using repeated medians, *Biometrika.,* **69,** 242–246.

Smirnov, M.Y., 2003. Magnetotelluric data processing with a robust statistical procedure, *Geophys. J Int.,* **152,** 1–7.

Takeda, M., 1997. Local time variation of geomagnetic transfer functions, *Geophys. J Int.,* **130,** 765–770.

Tapping, K.F., 2013. The 10.7 cm solar radio flux (F10.7), *Space Weather,* **11**(7), 394–406.

Tauber, S., Banks, R., Ritter, O. & Weckmann, U., 2003. A high-resolution magnetotelluric survey of the Iapetus suture zone in southwest Scotland, *Geophys. J Int.,* **153,** 548–568.

Vargas, J.A. & Ritter, O., 2016. Source effects in mid-latitude geomagnetic transfer functions, *Geophys. J Int.,* **204,** 606–630.

Weidelt, P. & Chave, D.A., 2012. *The Magnetotelluric Method,* 1st edn, Cambridge Univ. Press.